Full Paper

Applied Organometallic Chemistry

Received: 1 July 2008 Revised: 26 July 2008 Accepted: 28 July 2008 Published online in Wiley Interscience: 9 September 2008

(www.interscience.com) DOI 10.1002/aoc.1454

Metallic Li in carbonaceous nanotubes grown by metalorganic chemical vapor deposition from a metalorganic precursor

Mahua Das[a]*, C. Bittencourt[b], J-J Pireaux[b] and S. A. Shivashankar[a]

Metallic Li in carbonaceous nanostructures was obtained in high concentration (as much as 33.4%) through metalorganic chemical vapor deposition involving certain lithium–aminoalkyl moieties, which are formed *in situ*, by decomposition of a precursor containing both cobalt and lithium. The bimetallic complex containing both lithium and cobalt was characterized by IR spectroscopy, mass spectroscopy, nuclear magnetic resonance spectroscopy, elemental analysis and thermogravimetric analysis. X-ray photoelectron spectroscopy measurements performed on the as-grown films demonstrate that lithium can be stable in metallic form in such a film. Results of X-ray photoelectron spectroscopic analysis of the as-grown films are presented as direct evidence of the formation and stabilization of metallic lithium in carbon nanotubes. Carbon nanotubes, encapsulating metallic lithium, can potentially act as a miniaturized nanobattery. Such a battery would be potentially useful in the next generation of communication and remote sensing devices, where a pulse of current is required for their operation. In addition, with metallic lithium, having an effective nuclear magnetic moment, such materials can be envisioned to show potential applications in devices based on nuclear magnetic resonances.

Keywords: lithium aminoalkyl moiety; precursor; MOCVD; metallic lithium encapsulated in carbon nanotubes; X-ray photoelectron spectroscopy

Introduction

Lithium, the lightest solid element, is a soft, reactive metal with a low melting point.[1] It undergoes a large number of reactions with both organic and inorganic reagents. It reacts with oxygen to form the monoxide, Li_2O, and the peroxide, Li_2O_2. Lithium is the only alkali metal that reacts with nitrogen at room temperature to form a nitride, Li_3N, which is black. Lithium reacts readily with hydrogen at about 500 °C to form lithium hydride, LiH. The reaction of lithium metal with water is exceedingly vigorous. Lithium reacts directly with carbon to form the carbide, Li_2C_2. Lithium combines readily with the halogens, forming halides, accompanied by the emission of light. While lithium does not react with paraffin hydrocarbons, it does undergo addition reactions with arylated alkenes and with dienes. Lithium also reacts with acetylenic compounds, forming lithium acetylides, which are important in the synthesis of vitamin A. Lithium metal is soluble in liquid ammonia and is slightly soluble in the lower aliphatic amines, such as ethylamine. It is insoluble in hydrocarbons. In this context, stabilization of metallic lithium in a solid matrix remains a challenging problem.

Soon after carbon nanotubes were prepared in bulk by the arc discharge technique,[2] the suggestion was made that it might be possible to encapsulate elemental metals within the inner cores of the nanotubes. Such a proposal followed logically from the successful preparation of fullerenes containing endohedral metals.[3,4] The first crystalline materials inserted within single-walled carbon nanotubes (SWNT) were clusters and one-dimensional nanowires of Ru metal formed by immersing a sample of acid-treated SWNTs in a saturated solution of $RuCl_3$.[5] Following H_2 reduction, a filling of approximately 2–5% of all the observed SWNTs with Ru metal was observed. Acidification was considered necessary in order to open the tips of the SWNTs, which were assumed to be closed. Subsequently, SWNTs were filled without acidification by capillary wetting with molten mixtures of silver halides or mixtures of alkali halides and actinide halides.[6] The ability of molten material to wet and fill SWNTs depends on the wetting criterion determined by Ebbensen for the filling of nantubes with liquid phase media.[7] Elements such as Pb, Bi, Cs and S and Se were introduced by heating the element with open-ended nanotubes.[8–10] Capillary action and wetting play important roles in the process. In general, the filling procedure entails heating as-made nanotubes with the molten salts or oxides to a temperature 100 K above the melting point of the filling material. Improvements in filling yields (from 20–30% to more than 50–70%) can be achieved by thermally cycling the filling material from the filling temperature to 100 K below this temperature.[11] The excess filling material may be removed without removing the encapsulated material by gently washing the filled composite with cool or warm water, or with dilute HCl. Mixtures of predominantly amorphous ternary phase materials may similarly be introduced into the SWNTs by exploiting the melting properties of the relevant phases.[6] SWNTs can now be filled with a wide range of solid phase crystalline and noncrystalline materials including metals and metal salts,[5,6,12] oxides[13,14] and helical iodine chains.[15]

While nanotube-nanocrystal structures can be prepared[16–18] by a *multi-step* template carbonization technique in metalor-

* *Correspondence to: Mahua Das, Materials Research Centre, Indian Institute of Science, Bangalore-12, India. E-mail: dmahua2006@gmail.com*

a *Materials Research Centre, Indian Institute of Science, Bangalore-12, India*

b *University of Namur, LISE laboratory, 61, Rue de Bruxelles, B-5000, Namur, Belgium*

ganic chemical vapor deposition (MOCVD), there are very few reports in the literature on the fabrication through MOCVD of nanotube–nanocrystal heterostructures by a *one-step* route,[19] using a single molecular precursor and in the absence of any template. Schnitzler *et al*. showed[19] synthesis of iron and iron-oxide filled carbon nanotubes by a one-step route based on the pyrolysis of ferrocene or a ferrocene–$Fe_3(CO)_{12}$ mixture, using the MOCVD technique.

The encapsulation of metallic lithium in carbon nanotunse (CNT) has been unsuccessful in the past because of the very chemical nature of lithium metal, i.e. chemical reactivity of metallic lithium with ambient air, both O_2 and N_2. Hence procedures involving heating the metal with nanotubes, which are employed for metals such as Pb, Bi and Cs, could not be used in the case of lithium. The present work deals with incorporation of metallic lithium in high concentration in carbon nanotubes present in a film grown by low-pressure MOCVD using a single source metalorganic complex as precursor, in the absence of any reactive gas or a template. Under the chemical vapor deposition (CVD) conditions employed, the complex produces certain organometallic moieties *in situ* which subsequently result in the deposition of films rich in Li(0). The stabilization of metallic lithium in carbon nanotube, which is able to withstand pressure as high as 43 GPa, has been achieved. Thus stabilization of metallic lithium in a chemically, mechanically and thermally stable solid matrix such as a carbon nanotube will enable further investigations on this material.

Experimental

Synthesis of precursor $Li_2Co_2(teaH)_2(OAc)_3(OH)\cdot 2H_2O\cdot CH_3OH$

The precursor was synthesized as follows: 0.25 g of $LiOH\cdot H_2O$ was mixed in 20 ml of CH_3OH, and shaken, resulting in a white slurry. To this mixture, 0.8 ml of triethanolamine was added. Separately, 1.48 g of $Co(OAc)_2\cdot 4H_2O$ was dissolved in 20 ml of CH_3OH. To this solution, the slurry containing $LiOH\cdot H_2O$ was added. The reaction mixture was stirred in a round-bottom flask for 24 h under ambient conditions, whereupon a dark violet solution was obtained. The solution was then left at room temperature for 5 days in the same flask. The solvent was then removed using a rotary evaporator under vacuum, at 45–50 °C. The green gel-like mass obtained was then dried under vacuum and extracted with CH_2Cl_2. On keeping the extract at 4 °C for about 15 days, a solid dark violet product was obtained. The reaction pathway is given by equation (1):

$$2LiOH\cdot H_2O + 2Co(OAc)_2.4H_2O + 2(teaH_3) + Solv.(CH_3OH)$$
$$Li_2Co_2(teaH)_2(OAc)_3(OH).2H_2O.CH_3OH + HOAc + 9H_2O \quad (1)$$

Aspects of synthesis

It has been found that the dark violet solid product can be obtained only after aging the reaction mixture for several days, typically 5–6 days at room temperature. When solvent was removed from the reaction mixture immediately after the reaction had been completed, a dark violet gel-like mass was obtained. Extracting this with dichloromethane, and leaving the solution at 4 °C subsequently, led to slow decomposition of the product into a corresponding white lithium complex and pink cobalt complex. It was surmised that water acts as a 'molecular guard' to prevent interaction of polar dichloromethane molecules with the weakly coordinating OH-bond to Li. Such interaction, when allowed to take place, could be the plausible cause of decomposition of the product, as noted above.

Table 1. Conditions employed for CVD

Substrate	Stainless steel 316
Precursor	$Li_2Co_2(teaH)_2(OAc)_3(OH)\cdot 2H_2O\cdot CH_3OH$
Base pressure	0.2–0.3 m Torr
Working pressure	1 and 7 Torr
Substrate temperature	750 °C
Precursor vaporization temperature	55 and 63 °C
Carrier gas (Ar) flow rate	50 and 70 sccm
Reactive gas (O_2) flow rate	0 sccm
Deposition duration	90 min

Thin film deposition

Thin film deposition using this complex as precursor was carried out in a hot-wall, horizontal-flow reactor, using high-purity argon as the carrier gas, and in the absence of any reactive gas. An electronic mass flow controller (MFC) was used to regulate the gas flow. The heating of the precursor and the substrate was accomplished by (separate) resistive heating arrangements kept outside the quartz tube. The total pressure in the reactor was read by a capacitance manometer and was generally maintained in the range 1–10 Torr using a bellows-sealed throttle valve connected at the mouth of a rotary vane pump. The substrates (laser-cut pieces of 316 stainless steel, 1 mm in thickness and measuring 10 × 10 mm) were cleaned by soap solution, followed by distilled petroleum ether, and then boiled in distilled water, methanol and acetone, in that sequence. The deposition process was carried out for 90 min at a total pressure of 7 and 1 Torr, at a substrate temperature of 750 °C, precursor vaporization temperature of 55 and 63 °C, and with carrier gas flow rates of 50 and 70 sccm. The CVD conditions employed are tabulated in Table 1.

Characterization of the Complex

The complex was characterized by infrared spectroscopy, mass spectroscopy, elemental analysis, and by simultaneous thermogravimetric and differential thermal analysis.

IR spectroscopy

The IR spectrum of the complex in a KBr pellet was recorded between 4000 and 400 cm^{-1} (Fig. 1). The very broad band at

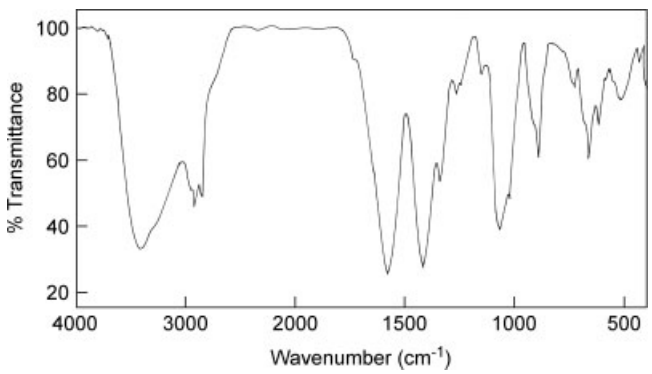

Figure 1. Infrared spectrum of the complex.

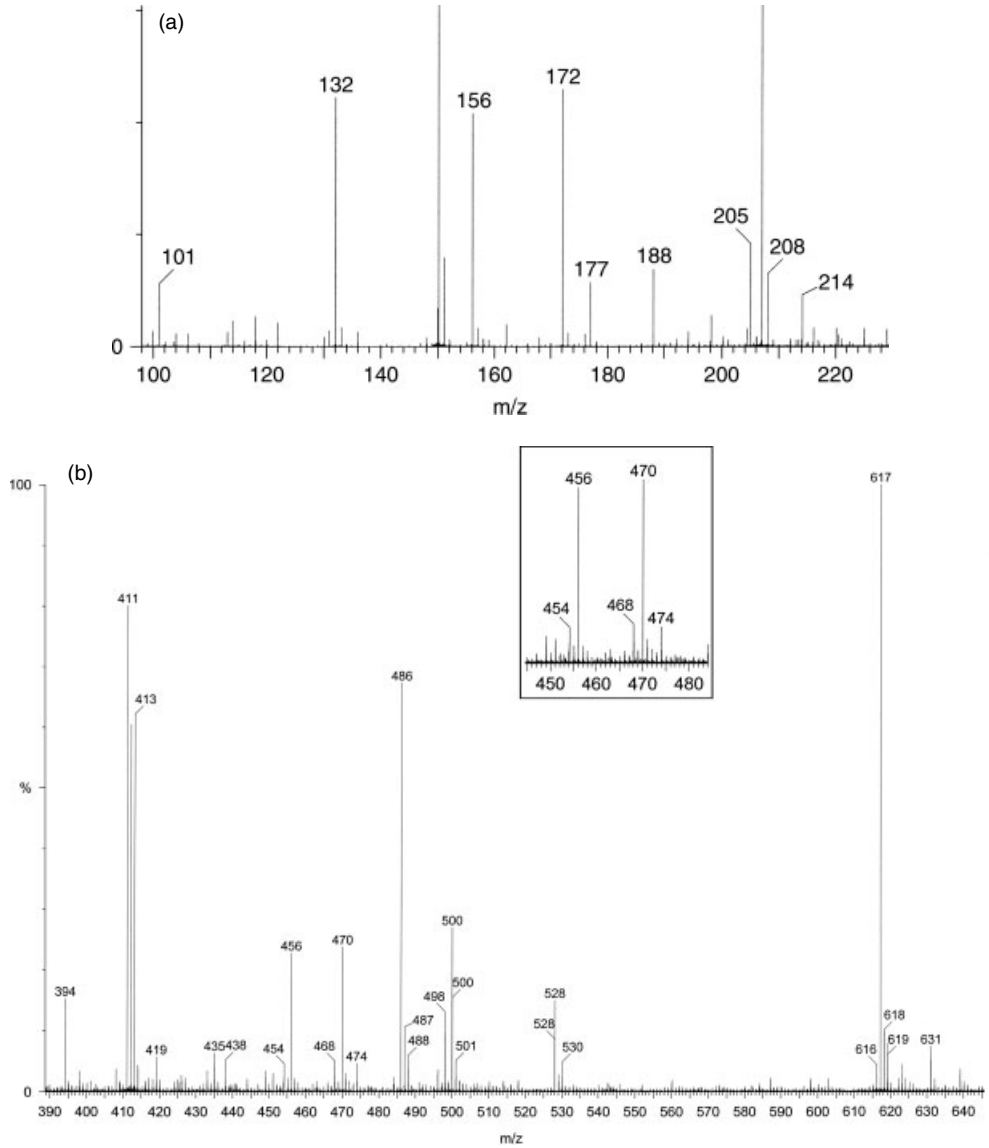

Figure 2. Mass spectra of the complex.

3404 cm^{-1} is due to the hydrogen-bonded O–H stretching vibration. The medium band at 1342 cm^{-1} is due to the C–N stretching vibration of the ligand triethanolamine. The strong band appearing at 1572 cm^{-1} is due to hydrogen bonded C═O stretching vibration of the acetate moiety. A weak band near 1750–1735 cm^{-1} appearing in the spectrum probably results from Fermi resonance between the C═O band of acetate and the overtone band of the band near 894 cm^{-1}. The C–H stretching vibrations of the methylene moiety were observed by strong and sharp bands at 2924 and 2855 cm^{-1}; the strong band appearing at 1415 cm^{-1} is due to the C–H bending mode. The out-of-plane C–H bending vibrations occur in the range 675–900 cm^{-1}. The strong bands observed at 1065 and 1023 cm^{-1} can be attributed to C–O stretching vibrations in methanol and triethanolamine.

Mass spectroscopy

The mass spectrum of the complex was recorded in the quick time-of-flight (QTOF) positive ion electrospray mode in methanol. The spectrum shows a well-resolved isotope distribution pattern. The assignment of different *m/z* values to various fragments was done based on their mass/charge ratio as well as the corresponding isotope distribution pattern. It is to be noted that two chemically different species can have the same *m/z* ratio, but their isotope distribution patterns are always different. Thus, isotopic distribution is the fingerprint of a particular chemical species. It has been found that the *m/z* values and the isotope distribution pattern obtained from the experimental mass spectra of the complex match well with the calculated ones. Figures 2 and 3 show the experimental and the calculated isotope distribution pattern, respectively. The calculated *m/z* values displayed in Fig. 3 correspond to the Li-7 and Co-59 isotopes.

The peak at $m/z = 101$ is due to the fragment $Li(CH_2CH_2)NLi(CH_2CH_2OH)$. The peak at $m/z = 132$ corresponds to the moiety $LiC_{10}H_5$; the one at $m/z = 130$ is due to the moiety $C_{10}H_5$. The peaks at $m/z = 150$ are superimposed or overlapped distribution patterns from two different species, one of which is due to the moiety $Li_4NC_8H_{13}$ and the other due to the fragment $teaH_3$; the one with a smaller height is due to the moiety $Li_4NC_8H_{13}$.

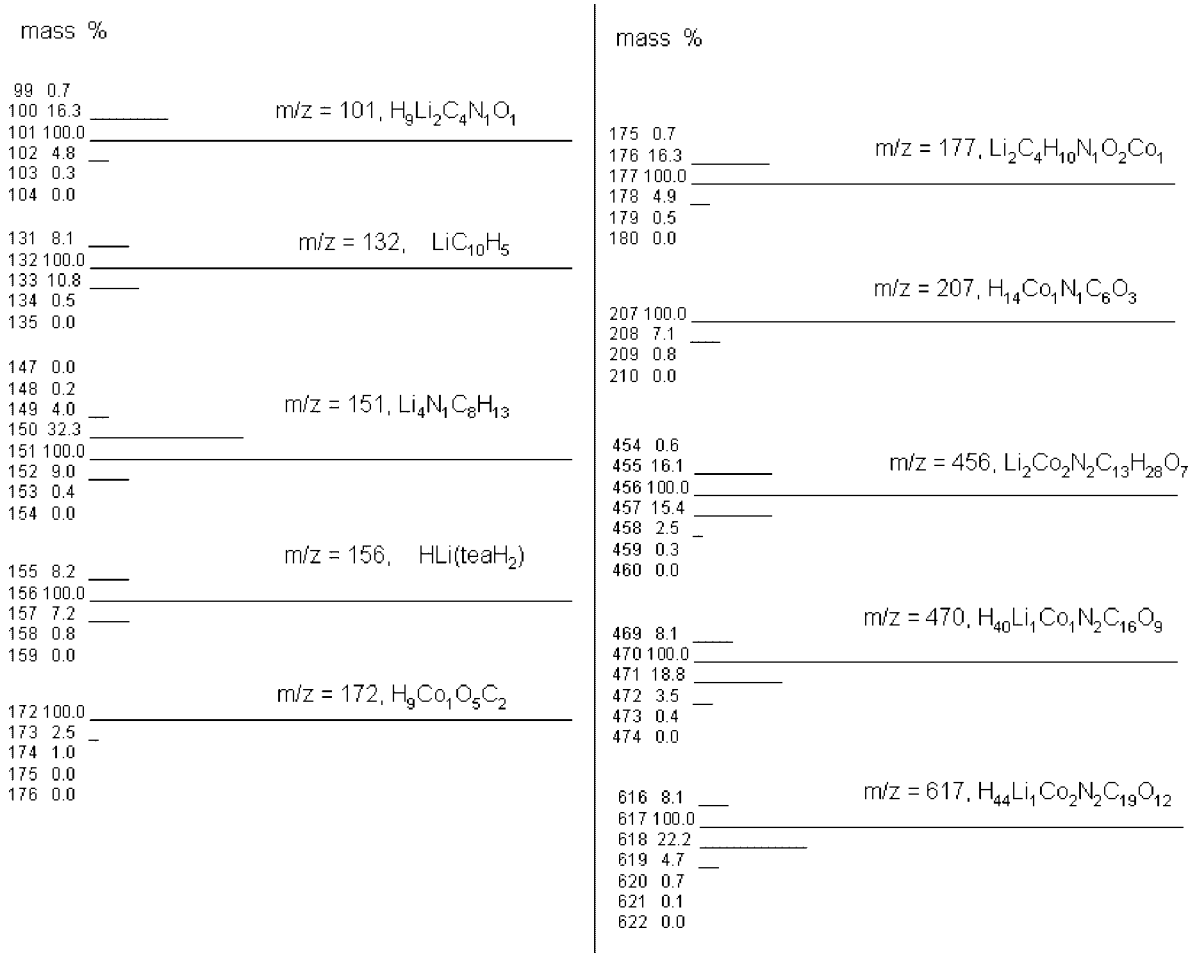

Figure 3. Calculated mass spectra of the complex.

Table 2. Lithium metal containing fragments

m/z	Moiety
101	$Li(CH_2CH_2)NLi(CH_2CH_2OH)$
132	$LiC_{10}H_5$
151	$Li_3NLiC_8H_{13}$

The peaks at $m/z = 172$ and $m/z = 207$ can be attributed to the moiety $HCo(OAc)(OH)(H_2O)_2$ and $HCo(teaH)$, respectively.

Many peaks reveal the presence of bimetallic Li and cobalt in the respective moieties. The peak at $m/z = 177$ is due to the fragment $Li(CH_2CH_2)NLi(CH_2CH_2OH)Co(OH)$. The peaks at $m/z = 456$ and $m/z = 470$ correspond to the fragments $Li_2Co_2(tea)_2(CH_3OH)$ and $HLiCo(teaH)(OAc)(CH_3OH)_2N(CH_2CH_2OH)_2(CH_2CH_3)$, respectively. The peak observed at $m/z = 617$ corresponds to the fragment $HLiCo_2(tea)(OAc)_2N(CH_2CH_2O)_2(CH_2CH_3)(CH_3OH)_3$. The fragment containing only lithium metal, which corresponds to the isotope Li-7, is tabulated in Table 2.

It is noteworthy that the mass spectrum of the complex does not show the expected pattern due to the moiety $HLi(teaH_2)$. The isotope distribution pattern of the peak observed at $m/z = 156$ does not match with that of $HLi(teaH_2)$. This suggests two possibilities: (1) that Li is not present in alkoxide form in the complex; and (2) that the $HLi(teaH_2)$ is extremely unstable to be determined my mass spectroscopy and under the applied voltage undergoes reaction to form a stabler $LiC_{10}H_5$ moiety.

Elemental analysis

The elemental analysis was carried out both for the lighter elements (C, H, N) and for the metals (Li and Co). The found values of (C, H, N) are as follows: C, 32.9; H, 6.19; N, 4.05. The values calculated for $Li_2Co_2N_2C_{19}H_{44}O_{16}$ are as follows: C, 33.13; H, 6.39; N, 4.06, which are in close agreement with the experimental values.

The metallic content in the complex was determined by the inductively coupled plasma analysis (ICP), an analytical technique used for the detection of trace metals in environmental samples. The primary goal of ICP is to get elements to emit characteristic light, which can then be measured. The light emitted by the atoms of an element in the ICP must be converted to an electrical signal that can be measured quantitatively. This is accomplished by resolving the light into its components (nearly always by means of a diffraction grating) and then measuring the light intensity with a photomultiplier tube at the specific wavelength for the line(s) characteristic of each element present in the analyte. The light emitted by the atoms or ions in the ICP is converted to electrical signals by the photomultiplier in the spectrometer. The intensity of the electronic signal is compared with previously measured intensities of a standard, thus allowing computation of its concentration in the analyte. Each element will have many

Table 3. ICP analysis of metals

Run	Label	Time	7Li(ppm)	59Co(ppm)
1	Tea21	4:40:19 pm	(P)13.920	(M)2042.000
2	Tea21	4:41:50 pm	(P)13.950	(M)2065.000
3	Tea21	4:43:21 pm	(P)3.572	(M)554.600
	Mean of Tea21		(P)10.480	(M)1554.000
	SD of tea21		(P)5.984	(M)865.500
	%RSD of tea21		(P)57.090	(M)55.700

specific wavelengths in the spectrum which could be used for analysis.

For ICP analysis, the precursor sample was digested in a high-purity (nitric acid + hydrogen peroxide + perchloric acid) reagent. Upon complete digestion, the precursor is completely destroyed. The entire organic moiety, whatever it may be, is converted into CO_2, NO_2 and H_2O. The digested solution is further diluted 2000-fold in 2% HNO_3 for injection into the ICP-MS analyzer. The results of the analysis in terms of pulse count (P) are shown in Table 3.

Table 3 shows that data recorded after an elapsed period of ~2 min differ significantly. For example, for cobalt, the standard deviation is 865 ppm; for Li the standard deviation is 6 ppm. Such inconsistency in the data suggests that, prior to analysis being carried out, i.e. during digestion, some of the lithium was removed as volatile species, along with organic components, resulting in a lower concentration of lithium and a higher concentration of cobalt in the solution than calculated. The metallic contents of Co and Li in the complex are as follows: found, Co, 15.2%; Li, 1.775%. Calcd, Co, 17%; Li, 2%.

Nuclear magnetic resonance spectroscopy

The nuclear magnetic resonance (NMR) spectrum of the complex was recorded in CD_3OD using a 400 MHz Bruker spectrometer. The proton NMR spectrum of the complex is shown in Fig. 4. The spectrum consists of four broad peaks at $\delta = 3.12, 3.42, 3.47, 3.64$ ppm. A nucleus in the vicinity of an electronegative atom experiences reduced electron density and the nucleus is therefore de-shielded. The nucleus in the vicinity of a more electronegative atom will, therefore, show higher δ values. The assignment of chemical shifts to different protons of the triethanolmine anion bonded to cobalt is shown in the inset of Fig. 4. The ones at δ 3.12 and δ 3.42 correspond to the $-NCH_2$ group, and the ones at δ 3.47 and δ 3.64 correspond to the OCH_2 group, respectively. The observed values for $-NCH_2$ and $-OCH_2$ match well with those reported for triethanolamine complexes.[20] The splitting of the peaks was obscured by the broadening of the peaks; the observed broadening might be due to the presence of paramagnetic Li^+ ion in the complex.

The most probable structures of the lithium-alkyl moieties

The most probable structures of the lithium-alkyl moieties, obtained upon decomposition of the precursor, are shown in Fig. 5. The presence of moiety $C_{10}H_{10}$, i.e bullvalene, should be noticed, evidenced by the appearance of the peak at $m/z = 130$ in the mass spectrum of the complex [Fig. 2(a)]. The bullvalene moiety is presumably formed by the dehydration reaction of triethanolamine with methanol during decomposition of the bimetallic complex. The reaction pathway is presented in equation (2)

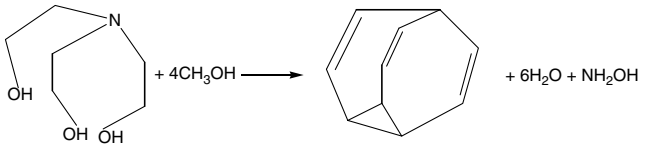

(2)

The $LiC_{10}H_5$ moiety is derived from the $Li(teaH_2)$ moiety through a similar reaction to that shown above.

Thermal analysis

Simultaneous thermogravimetric analysis (TGA) and differential thermal analysis (DTA) were carried out for the complex in flowing nitrogen, at a heating rate of 10 °C min^{-1}. The TGA/DTA plot is shown in Fig. 6(a). The first endothermic peak between 58 and 91 °C, as seen in the DTA curve, is due to the melting of the complex in that range of temperature. The weight loss of the precursor complex calculated from the TGA curve up to 60 °C is 2%, and that up to 100 °C is 5.57%.

The DTG (derivative thermogravimetry) curve [Fig. 6(b)] recorded together with TGA shows several peaks with variably intensity, which indicates the temperatures at which 'events' occur. The DTG curve shows a small peak centred at about 79 °C, which suggests that melting is accompanied by partial decomposition in this complex. The DTG curve shows additional broad peaks between 92 and 148 °C, and between 181 and 237 °C. An intense peak centred at 342 °C shows almost complete decomposition of the precursor.

Characterization of the Films

Transmission electron microscopy

Transmission electron microscopy along with selected area electron diffraction (SAED) was carried out to elucidate the nanotube structure. Figure 7 shows the bright-field transmission electron micrographs of the film grown at a pressure of 7 Torr, at various magnifications. The image at a magnification of 50,000 [Fig. 7(a)] shows a bundle of nanotubes, each one approximately 20 nm in diameter, and encased in a conical jacket (marked by an arrow) that resembles a 'squid'. The one at 100,000 magnification shows [Fig. 7(b)] three distinctly different kinds of nanotubes: at the extreme right, one single bent and elongated nanotube ~20 nm in diameter is observed (marked by an arrow); towards the left, a bunch of several straight nanotube of a diameter less than 20 nm was observed; on the extreme left, again the nanotube encapsulated in a conical jacket was visible (marked by a circle). A view at a higher magnification of 200,000 shows nanoparticles around ~3–5 nm in dimension embedded in the tubule, which is 5 nm in diameter [marked by an arrow, Fig. 7(c)].

The selected area diffraction pattern of the film shows the presence of graphitic C, together with $LiOH·H_2O$ and LiOH phases, as shown in Fig. 7(d, e). The lattice spacings obtained from the SAED pattern of the film were compared with JCPDS file nos 76–1074, 76–0911, 15–0401 and 75–1621. For the tubular feature, the reciprocal space consists of annular rings and disks.[21] The d_{002} lattice spacing of the nanotube was found to be is 3.4 Å, which matches well with the reported value of

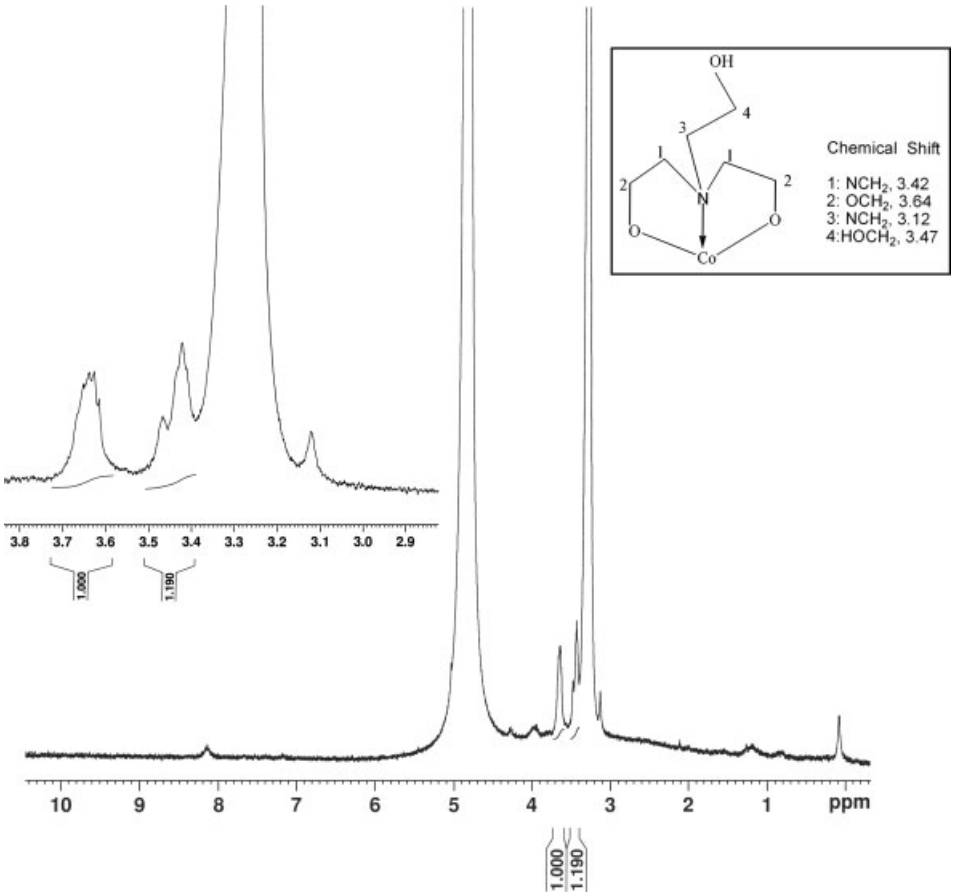

Figure 4. ^{1}H NMR spectrum of the complex.

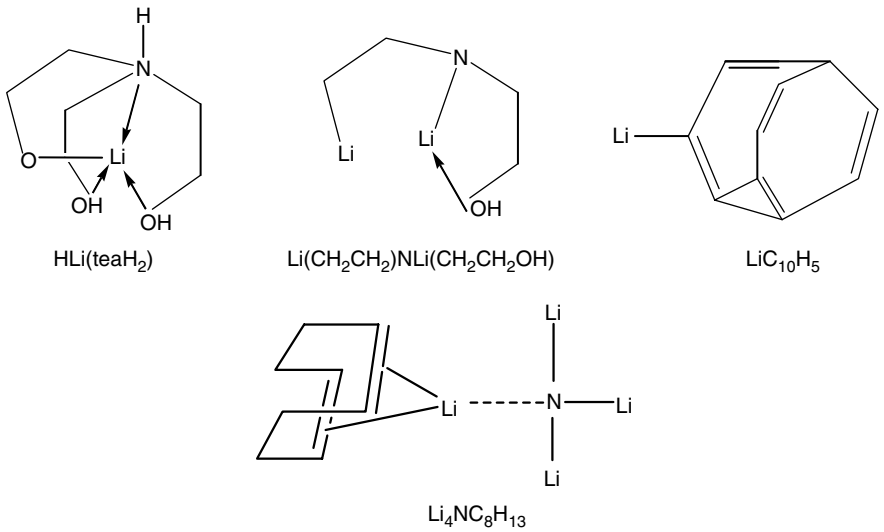

Figure 5. The most probable structures of the lithium-alkyl moieties.

nanotubular hexagonal graphitic crystals; the lattice spacing of d_{103} of hexagonal graphite was found to be 1.54 Å. Similarly, the calculated d-spacing of approximately 2 Å corresponds to the d_{101} spacing of 2.039 Å in hexagonal graphite. For one of the rings consisting of disks [Fig. 7(e)], the distance between origin and the position of the disks was found to be approximately 2.63 Å; this value corresponds to 2.65 Å, of d_{220} in monoclinic $LiOH{\cdot}H_2O$. From the disk shape of the diffraction patterns that correspond to (220) planes of $LiOH{\cdot}H_2O$, it is evident that $LiOH{\cdot}H_2O$ is present as tubules in the film. The distance of 2.42 Å corresponds to 2.42 Å, of d_{021} of the $LiOH{\cdot}H_2O$ phase. The d-spacing of 4.25 Å, which corresponds to the innermost ring, has been assigned to the d_{001} plane of tetragonal LiOH, as shown in Fig. 7(e). The reported value for d_{001} spacing of this phase is 4.33 Å. It is

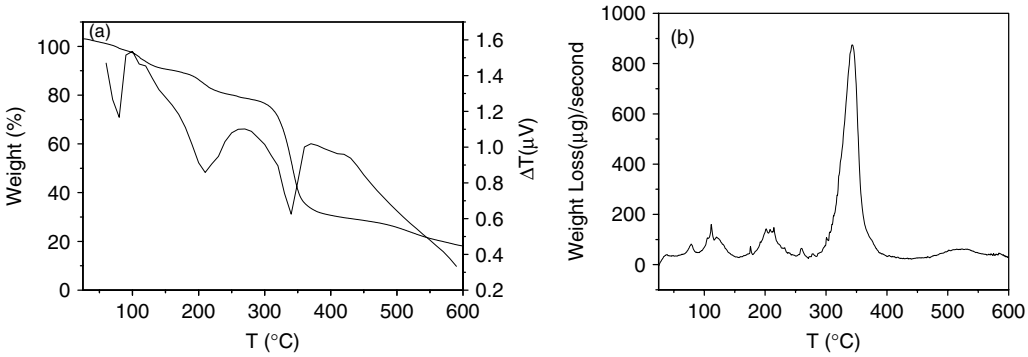

Figure 6. Thermal behaviour of the complex; (a) simultaneous TGA/DTA plot, (b) DTG plot.

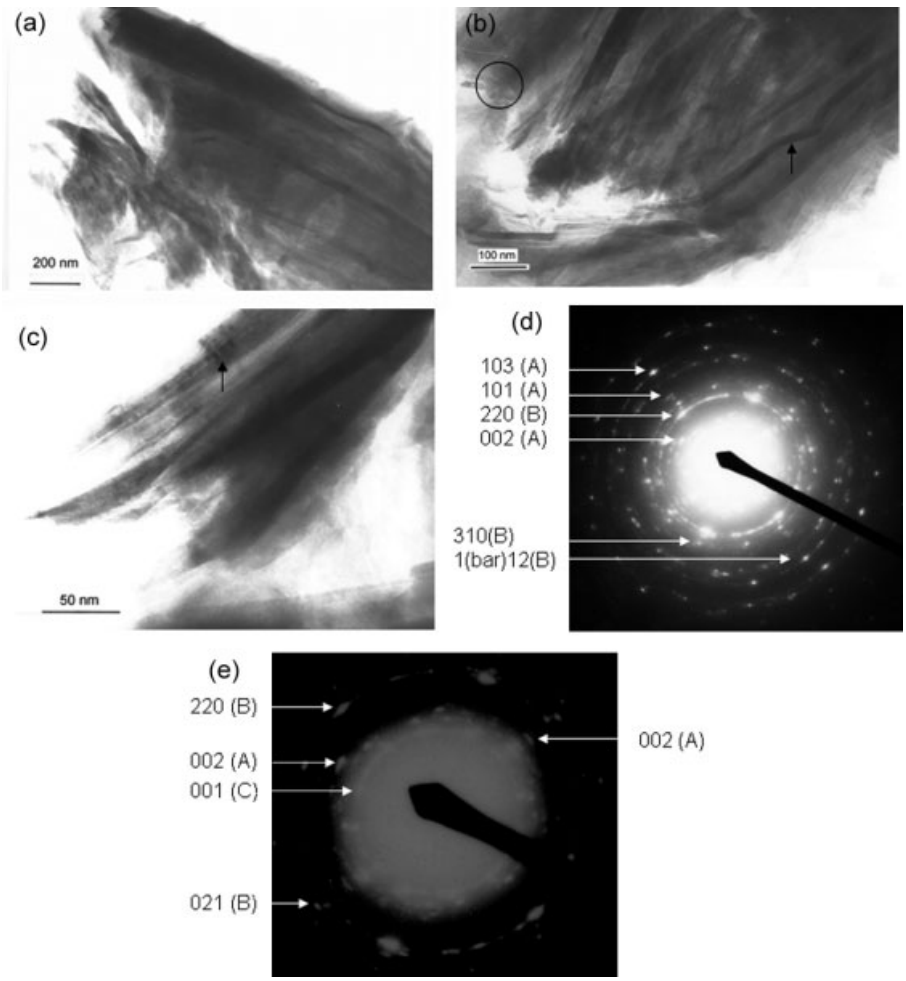

Figure 7. (a) Bright field TEM image of sample exhibiting hollow end of a carbon nanotube encased in a conical jacket; (b) TEM micrograph of the film at 100,000 magnification; (c) TEM micrograph of the film at 200,000 magnification; (d) SAED pattern of the film shown in (b), consisting of several disks characteristic of tubular symmetry in the structures, together with dots. A = hexagonal graphite; B = $LiOH{\cdot}H_2O$; C = LiOH. (e) An enlarged view of the SAED pattern shown in (d) near the centre.

noteworthy that the innermost ring consists of several dots, from which it is evident that LiOH is present as nanocrystallites in the film.

It is to be noted that the d_{110} spacing of metallic lithium is 2.48 Å; however, given the condition of preparation of the TEM grid, using acetone as the solvent (which can contain some water, even when dried), the presence of metallic lithium in the TEM sample is quite unlikely.

X-ray photoelectron spectroscopy

Figure 8(a–f) shows the X-ray photoelectron spectra of the as-grown films. The films were grown at a reactor pressure of 7 Torr and 1 Torr, at a growth temperature of 750 °C. Figure 8(a–c) shows the XPS spectra of the film grown at a reactor pressure of 7 Torr; Fig. 8(d–f) shows the XPS spectra of the film grown at the lower reactor pressure of 1 Torr.

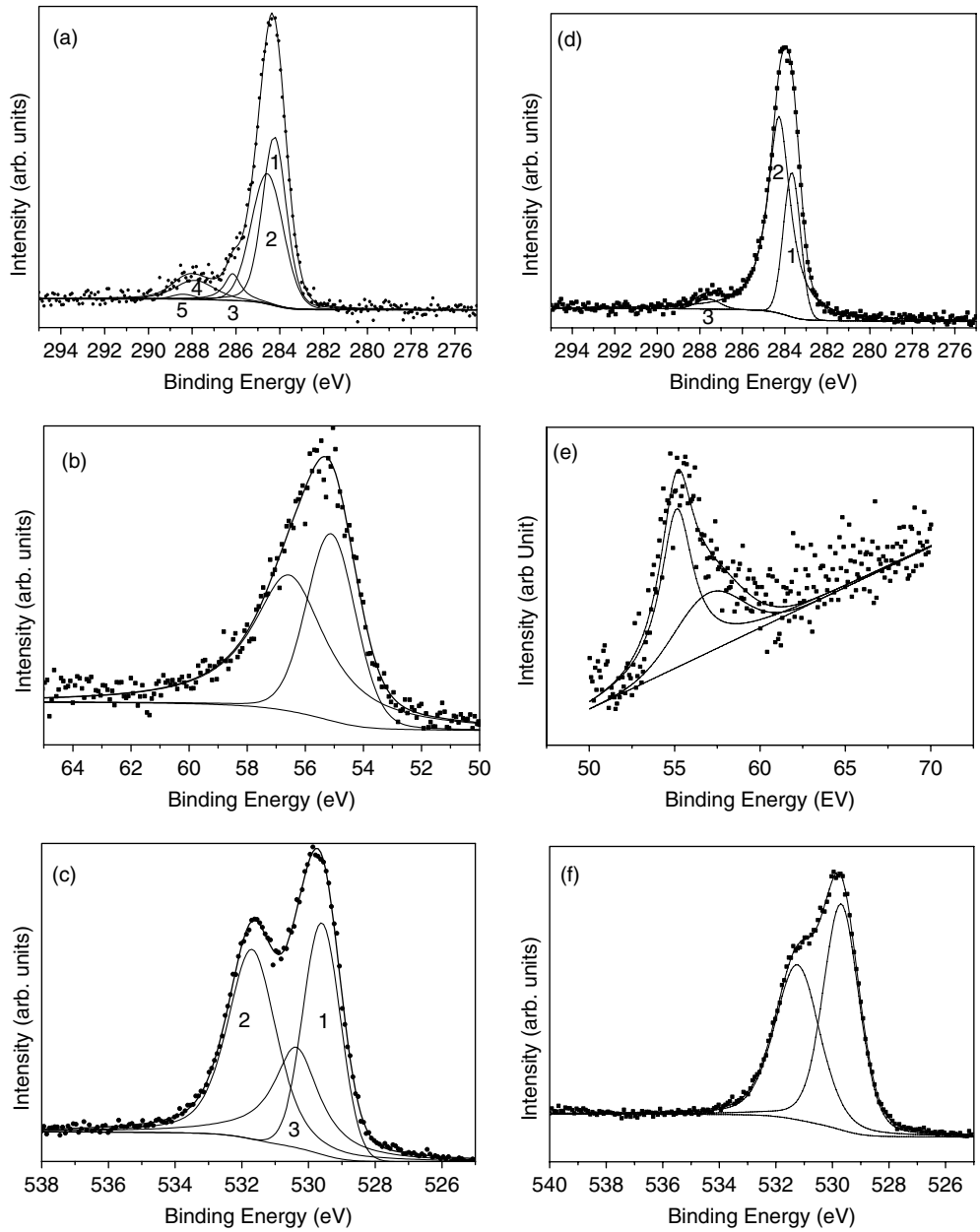

Figure 8. XPS of the films grown at different reactor pressures: (a–c) pressure 7 Torr; (d–f) pressure 1 Torr.

Figure 8(a) shows the C1s line of the as-grown film of the corresponding film. The spectrum can be decomposed into five components. The main component (1) at 284.3 eV corresponds to the graphite signal, assuming a pure nanotube similar to a graphite layer.[22] The second component centred at 285.0 eV is attributed to the sp^3 carbon atoms. The components centred at 286.2 eV (3), 287.9 eV (4) and 288.4 eV (5) correspond to hydroxyl,[23] carbonyl (or ether),[24] and carboxyl (or ester) groups, respectively.[25]

The C1s peak is very similar to the one reported[26] for carbon nanotubes functionalized in oxygen plasma, the difference arising in the amorphous carbon component. The R═C═O radicals are attached to the nanotube and nano-squid surface in the present case. The reported value for free CO_3^{2-} species is at 290.2 eV,[27] while that for the C1s peak in Li_2CO_3 is reported to be 290 eV. It is noteworthy that the C1s peak does not show any component corresponding to carbonate CO_3^{2-} species.

The Li (1s) spectrum [Fig. 8(b)] can be decomposed in two components, one centred at 56.5 eV and the other at 55.1 eV. The peak broadening observed at higher binding energy region was attributed to –OH located on different sites. The fitted pattern centred at 55.1 eV shows considerable asymmetry, resembling that observed for metallic lithium (Li°).[28] While the reported value for metallic lithium is at 54.8 eV, that reported for Li_2CO_3 is at 55.0 eV, with a fairly symmetric peak reported for the latter. The Li1s peak, surprisingly, does not show any component corresponding to Li_2O, for which the reported value is 53.3 eV. The component at 56.5 eV can be attributed to LiOH. The O1s spectrum of the corresponding film is shown in Fig. 8(c). The O1s spectrum resembles that observed for carbon nanotubes functionalized with oxygen. This spectrum can be decomposed into three components at 529.6 eV(1), 530.4 eV(2) and 531.7 eV(3), respectively. The component with resolved energy at 529.6 eV may

be attributed to the presence of hydroxyl (OH) species or adsorbed O, for which the reported value is 529.7 eV. The component at 531.7 eV may be attributed to the presence of carbonyl group, C═O, for which the reported value is 531.6 eV. The component at 530.4 eV is associated with O1s in LiOH.

The XPS spectra of the film grown at a reactor pressure of 1 Torr are shown in Fig. 8(d–f). The C1s peak [Fig. 8(d)] can be decomposed into three components with resolved energies of 283.6 eV(1), 284.2 eV(2) and 287.6 eV(3). The component at 283.6 eV corresponds to the moiety $-(C^*H_2\text{-}CH_2)_n$.[29] The component at 284.2 eV corresponds to graphitic carbon. The low intensity broad component at 287.6 eV is due to the –C═O– moiety. The shape of the component at 284.2 eV is quite unlike that of pure graphite and pretty much similar to that observed for lithium graphite, LiC_6. An explanation of the asymmetric line shape for metals has recently been given in terms of a final excitonic screening mechanism. When a core electron is suddenly removed from an atom in a metal, and a unit positive charge (core hole) suddenly appears, the response of the electron subsystem changes, which results into electron–hole pairs. The mechanism of the creation of the (e–h) pairs was proposed by Anderson[30] and Mahan.[31] They showed that the sudden photo-ionization-induced appearance of a long-lived hole (localized disturbance) on the core level leads to the creation of e–h pairs with very low energy and high momentum, in the electron gas, near the Fermi level. Since the core hole has infinite effective mass, and hence can absorb arbitrarily high momentum, a large number of such pairs are excited. In this case, the photoelectron spectrum is singular. It is tempting to decompose the LiC_6 line into a similar asymmetric peak plus a broad component at 1.4 eV greater in binding energy. The resulting LiC_6 line has a singularity index of 0.30, greater even than that of metallic lithium.[32]

The Li1s core level spectrum is shown in Fig. 8(e). The line shape of Li1s spectrum shows strong asymmetries resulting from metallic character. The Li1s peak for this film can be decomposed into two components, at 55.1 and 57.38 eV. The shape of the asymmetric component at 55.1 eV resembles that observed for lithium metal film.[28] Wertheim *et al*.[33] reported the peak for lithium graphite, LiC_6, at 57.38 eV. The binding energy of Li1s electron in LiC_6 is greater than that in metallic lithium. This is in accord with the expectation of a unit charge transfer from Li to graphite and, thus, Li is present in LiC_6 as a Li^+.

The observed line width of the Li(0) components has been found to differ significantly from that observed for a pure lithium metal film. The actual line width of Li (0) component was calculated by subtracting the instrumental broadening or response function of the instrument, which is 0.7 eV, from the observed FWHM of the Li(0) component. The calculated value of the FWHM of Li(0) components are 0.447 and 1.383 eV for the films grown at 1 and 7 Torr, respectively. The calculated values differ considerably from reported values for the line width for a pure metallic lithium film, which ranges from 0.24 to 0.35 eV,[28] depending on the temperature at which the XPS spectrum is recorded. The line width due to phonon broadening observed for pure metallic lithium film is reported to be 0.35 eV at 300 K. This suggests that a broadening mechanism, in addition to phonon broadening, is operative in the present case, which contributes to the enhancement of the line widths of the peaks due to metallic Li. In metals, the creation of low energy conduction electrons–hole pairs leads to an asymmetric broadening on the high binding energy side of an asymmetric peak.[34,35] The widths of the core hole states were shown to change dramatically with chemical environment. From this study, chemically dependent life time processes and interatomic Auger transitions were inferred to be responsible for the observed effects. According to the theory of Weisskopf and Wigner,[36] the life times of individual hole states should simply contribute additively to the widths of the emitted X-rays.

Table 4. Relative concentration of species in the film grown at 750 °C, 7 Torr, 50 sccm Ar

XPS line	Position (eV)	Width (eV)	Relative concentration (%)
C1s	284.3	1.234	6.23
	285.0	1.683	6.05
	286.2	0.841	2.49
	287.9	2.188	2.67
	288.4	1.066	0.36
O1s	529.6	1.402	9.3
	530.4	1.395	2.47
	531.7	1.808	9.2
Li1s	56.5	3.135	26.5
	55.07	2.083	33.4

Table 5. Relative concentration of species in the film grown at 750 °C, 1 Torr, 70 sccm Ar

XPS line	Position (eV)	Width (eV)	Relative concentration (%)
C1s	283.6	0.939	7.4
	284.2	1.267	19.78
	287.6	1.32	0.72
O1s	529.69	1.495	14.9
	531.24	1.864	13.2
Li1s	55.12	1.147	27.7
	57.38	4.625	15.7

The relative elemental concentrations of the films were calculated, and were found to be as follows, Li 60%, O 21%, C 17.8%, N 0% and Li 43.5%, C, 27.9%, O, 28.3%, N 0%, for the films grown at 7 and 1 Torr, respectively. Quantitative XPS shows that there were no nitrogen-containing moieties present in the film. The relative concentrations of different species in the films, their positions and line widths of the corresponding components are shown in Tables 4 and 5. It is noteworthy that the percentage of lithium in the film can be as high as three times that of oxygen. This large difference between the elemental concentrations of lithium and oxygen complements the presence of the extra lithium in the Li (0) state. The relative concentration of carbon is almost equal to that of oxygen in both the films, suggesting that the surface of the nanotubes is functionalized with O species. For the film grown at reactor pressure of 7 Torr, the relative concentrations of the components at 56.5 and 55.0 eV are 44.2 and 55.7%, respectively. From this, 33.4% lithium was estimated to be in the Li(0) state. For the film, grown at reactor pressure of 1 Torr, the relative concentrations of the components at 55.1 and 57.38 eV are 63.8 and 36.1%, respectively; i.e. the relative concentration of metallic lithium in this film is 27.7%.

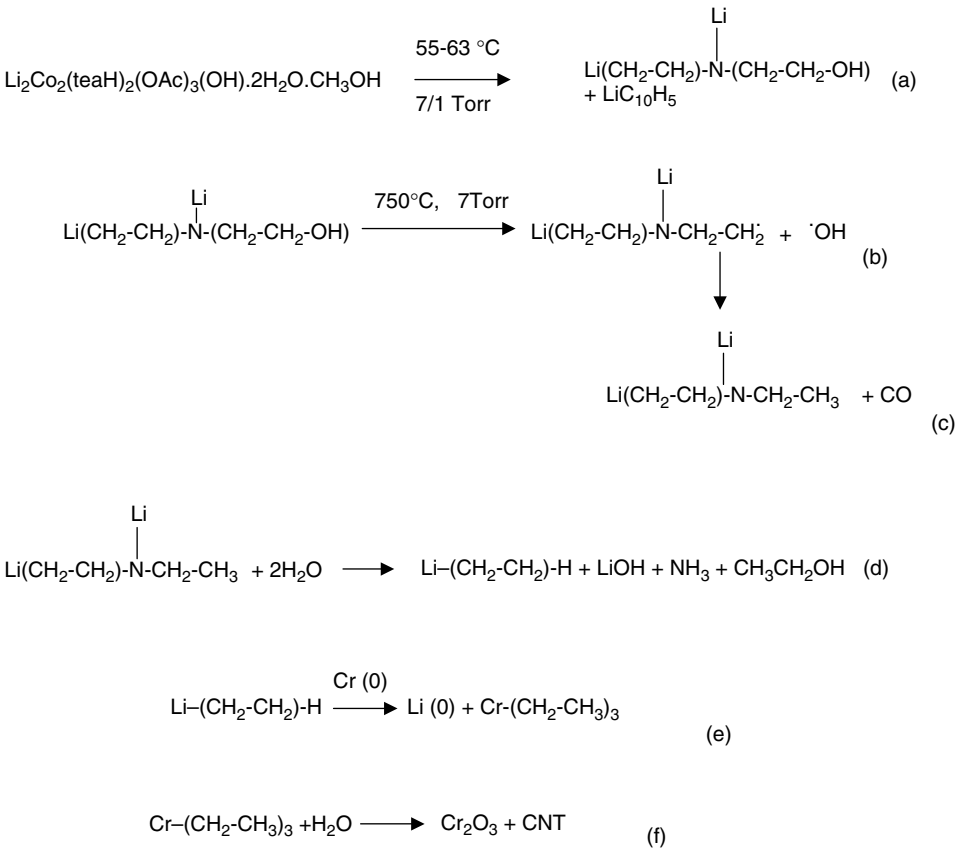

Scheme 1. Mechanism of growth through radical formation.

Proposed Mechanism of Growth

The growth mechanisms of CNTs remain somewhat controversial despite all the efforts made both experimentally and theoretically to validate competing theories.[37] However, a few basic steps are generally acknowledged in the chemical CNT formation, regardless of whether the growth takes place in the gas phase or on a support surface. The catalytic decomposition of the carbon precursor molecules on the surface of the metal catalyst particles is followed by diffusion of the released carbon atoms into the metal particles. Carbon saturation in the metal occurs either by reaching the carbon solubility limit in the metal at a given temperature or by lowering the solubility limit via a temperature reduction. Supersaturation results in solid carbon precipitation from the metal particles.

Interesting and useful insight towards understanding the growth mechanism of carbon nanotube and carbon nanosquid rich in Li(0), realized experimentally in the present study, can be obtained by a comparative study of TGA of the complex, mass spectra of the precursor, and X-ray photoelectron spectra of the grown films. The carbon nanotubes rich in metallic lithium were formed by partial decomposition of the precursor $Li_2Co_2(teaH)_2(OAc)_3(OH)\cdot 2H_2O\cdot CH_3OH$, under the CVD conditions employed in the present study. The experimentally determined melting temperature of the precursor was 73 °C under ambient conditions. The simultaneous TGA/DTA curve [Fig. 6(a)] reveals that the melting is followed by decomposition. Under the reduced pressure of 1 and 7 Torr, the precursor first melts and then decomposes. The weight loss of the precursor calculated from TGA curve is 2% up to 60 °C and 5.57% up to 100 °C. The weight loss of 5.57% corresponds to the removal of the $Li\text{–}(CH_2\text{–}CH_2)\text{–}H$ moiety with equivalent weight loss of 5.23%. The $Li\text{–}(CH_2\text{–}CH_2)\text{–}H$ moiety results from further decomposition of $Li(CH_2CH_2)NLi(CH_2CH_2OH)$ moiety, i.e. $H_9Li_2C_4N_1O_1$, which, in turn, results from the decomposition of the precursor. The formation of the $H_9Li_2C_4N_1O_1$ moiety is revealed by the mass spectrum of the complex (Fig. 2), which shows a peak at $m/z = 101$. Additional evidence of formation of $Li\text{–}(CH_2\text{–}CH_2)\text{–}H$ species comes from the presence of $\text{–}(CH_2\text{–}CH_2)\text{–}$ species (7.4%) in the film grown at a pressure of 1 Torr, as evident from the C1s peak of the XPS spectra of the corresponding film. The peak at $m/z = 177$ corresponds to the fragment $[Li(CH_2CH_2)NLi(CH_2CH_2OH)Co(OH)]^+$. The calculated isotope distribution pattern (Figure 3) of these fragments matches the experimentally observed pattern, which provides additional evidence for the formation of the $H_9Li_2C_4N_1O_1$ moiety during CVD process. This suggests that the $Li\text{–}(CH_2\text{–}CH_2)\text{–}H$ moiety, formed *in situ*, through decomposition, vaporizes and contributes to the formation of the nanotube and nanosquid structure together with copious amount of metallic lithium. This is again consistent with the presence of a trace amount (1%) of cobalt in the film, as determined by XPS. It is to be noted that at substrate temperature as high as 750 °C, metallic Cr can sublime from the substrate stainless steel, which assists the reduction of Li^{+1} state in $Li\text{–}(CH_2\text{–}CH_2)\text{–}H$ to Li(0) state. As a result, metallic Cr gets oxidized to Cr_2O_3 and forms a buffer layer. Such a mechanism is supported by presence of trace amount of Cr_2O_3 in the depth profile of the film, as revealed by XPS data obtained after sputtering the film for 30 min. A possible reaction mechanism is outlined in Scheme 1.

At high temperatures, the OH radical decomposes on a catalyst surface from an alcohol, and attacks the nearby carbon atoms

with dangling bonds to form CO.[38] It is to be noted that the presence of carbonyl species or hydroxyl species attached to carbon is negligible, as revealed by the C1s spectra. This supports the proposed mechanism in step (c) of Scheme 1. The film grown at the reactor pressure of 1 Torr is free of LiOH, whereas the film grown at 7 Torr comprises LiOH, suggesting that the lithium alkyl moiety involved is mostly $LiC_{10}H_5$ when the deposition is carried out at a pressure of 1 Torr, using higher precursor vaporization temperature of 63 °C and higher carrier gas flow. Therefore, it seems that, at a higher vaporization temperature, formation of $LiC_{10}H_5$ moiety is predominant over formation of the $Li(CH_2CH_2)NLi(CH_2CH_2OH)$ moiety.

At the lower pressure of 1 Torr, the velocity at which the molecules strike the substrate is greater than that at the higher pressure of 7 Torr. On the contrary, the lower vaporization temperature and the smaller carrier gas flow rate, employed when the deposition was done at higher reactor pressure of 7 Torr, both contribute to the reduction in the flux of precursor molecules.

Since chromium can form a wide range of organometallic complexes, of which many typically violate the 18 electron rule,[39] it is impossible to predict the exact nature of intermediate species. Scheme 1 represents a likely mechanism for the formation of CNT rich in Li(0) through a probable Cr–alkyl intermediate. It is notable that the as-grown film at a reactor pressure of 1 Torr is free of LiOH. This suggests that the formation of Li(0) is a kinetically favoured process under the CVD conditions employed. It is noteworthy that, from the quantitative XPS, the presence of 1% cobalt was determined in the as-grown films. In this context, the functionality of a Cr–Co bimetallic catalyst in the formation of CNTs or the synergistic effect of both chromium- and cobalt-containing species as catalysts in the overall growth process, cannot be ruled out.

Seemingly, the formation of ethyl lithium in the surroundings of coordinating water is unlikely, as lithium alkyls are known to be very reactive to water. However, in case of the coordinating water engaged in hydrogen bonding, such intramolecular reaction may be prevented. Interference of coordinating water during formation of ethyl lithium may also be prevented due to specific conformation, which the molecule prefers to adopt. Evidence of hydrogen-bonded water has been obtained from the IR spectrum of the complex as shown in Fig. 1. The IR spectrum of the complex shows a broad peak at ~3400 cm^{-1}. The prevention of coordinating water from engaging in intramolecular reaction is plausible due to the relatively low vaporizer temperature (55–63 °C), maintained during CVD in the present study.

Potential Areas of Applications

Stabilization of metallic lithium in a solid matrix such as a carbon nanotube, which has high thermal, mechanical, chemical and physical stability, is a technologically important result in view of the low chemical stability and the high-pressure superconductivity[40,41] of metallic Li. In theory, the surface area of individual carbon sheets can be[42] as high as 2630 $m^2\ g^{-1}$, assuming that both sides of the sheets are accessible. A carbon nanosquid with no end caps may be expected to possess a large surface area. The typical nanosquid structure could potentially be useful for hydrogen storage and for supercapacitor applications. This novel C–C composite material can potentially be useful as heat-resistant thermal coating for re-entry space vehicles. The novel approach of using metalorganic complex as CVD precursor, in presence of an alkali metal, can be exploited in a variety of ways, each of which can potentially lead to numerous new and unusual CNT-based composite structures.

In the current state of the art of rechargeable batteries, metallic lithium acts as one of the electrodes. In this kind of anodic hollow fibre with cathodic core nanostructure, the diffusion distance of Li between cathode to anode and vice versa is expected to be extremely short (of the order of a few nm). As a result, diffusion time could be of the order of a few nanoseconds. Under an applied voltage, if there is a selective migration of Li–ion between the core and the wall with no tunneling of electrons taking place, it is likely to enhance the rate capability of the Li-ion rechargeable battery to a significant extent. Such a battery would be useful in the next generation of communication and remote sensing devices, where a pulse of current is required for their operation. In such a battery, each nanotube, encapsulating metallic lithium, would act as a miniaturized nanobattery.

Conclusions

1. Metallic Li in carbonaceous nanostructures were obtained in high concentration (as much as 33.4%) through MOCVD involving $Li(CH_2CH_2)NLi(CH_2CH_2OH)$ and $LiC_{10}H_5$ moieties, which are formed *in situ*, by decomposition of a precursor containing both cobalt and lithium.
2. The bimetallic precursor was characterized by infrared spectroscopy, mass spectroscopy, elemental analysis, and thermal analysis.
3. The as-grown films were characterized by X-ray photoelectron spectroscopy and transmission electron microscopy.
4. Such films have potential applications in high-pressure superconductivity and several other areas where stabilization of metallic lithium in a solid matrix, which is chemically, thermally and mechanically stable, such as CNT is required.

References

[1] J. D. Lee, *Concise Inorganic Chemistry*. Blackwell: Oxford, **1999**, pp. 288–291.
[2] S. Ijima, *Nature* **1991**, *354*, 56.
[3] J. R. Heath, S. C. O'Brien, Q. Zhang, Y. Liu, R. F. Curl, H. W. Kroto, F. K. Tittel, R. E. Smalley, *J. Am. Chem. Soc.* **1985**, *107*, 7779.
[4] S. C. O'Brien, J. R. Heath, R. F. Curl, R. E. Smalley, *J. Chem. Phys.* **1998**, *88*, 220.
[5] J. Sloan, J. Hammer, M. Zweifka-Sibley, M. L. H. Green, *J. Chem. Soc., Chem. Commun.* **1998**, 347.
[6] J. Sloan, D. M. Wright, H. G. Woo, S. Bailey, G. Brown, A. P. E. York, K. S. Coleman, J. L. Hutchison, M. L. H. Green, *J. Chem. Soc., Chem. Commun.* **1999**, 699.
[7] T. W. Ebbesen, *J. Phys. Chem. Solids* **1996**, *57*, 951.
[8] P. M. Ajayan, S. Iijima, *Nature* **1993**, *361*, 333.
[9] P. M. Ajayan, T. W. Ebbesen, T. Ichihashi, S. Iijima, K. Tanigaki, *Nature* **1993**, *362*, 522.
[10] E. Dujardin, T. W. Ebbesen, H. Hiura, K. Tanigaki, *Science* **1994**, *265*, 1850.
[11] G. Brown, S. R. Bailey, M. Novotny, R. Carter, E. Flahaut, K. S. Coleman, J. L. Hutchison, M. L. H. Green, J. Sloan, *Appl. Phys. A* **2003**, *76*, 1.
[12] J. Sloan, A. I. Kirkland, J. L. Hutchinson, M. L. H. Green, *J. Chem. Soc., Chem. Commun.* **2002**, 1319.
[13] J. Mittal, M. Monthioux, H. Allouche, O. Stephan, *Chem. Phys. Lett.* **2001**, *339*, 311.
[14] S. Friedrichs, J. Sloan, M. L. H. Green, J. L. Hutchison, R. R. Meyer, A. I. Kirkland, *Phys. Rev. B* **2001**, *64*, 045406.
[15] X. Fan, E. C. Dickey, P. C. Eklund, K. A. Williams, L. Grigorian, R. Buczko, S. T. Pantelides, S. J. Pennycook, *Phys. Rev. Lett.* **2000**, *84*, 4621.

[16] B. K. Pradhan, T. Toba, T. Kyotani, A. Tomita, *Chem. Mater.* **1998**, *10*, 2510.
[17] B. K. Pradhan, T. Kyotani, A. Tomita, *Chem. Commun.* **1999**, 1317.
[18] K. Matsui, B. K. Pradhan, T. Kyotani, A. Tomita, *J. Phys. Chem. B* **2001**, *105*, 5682.
[19] M. C. Schnitzler, M. M. Oliveira, D. Ugarte, J. G. Aldo Zarbin *Chem. Phys. Lett.* **2003**, *381*, 541.
[20] A. A. Naiini, V. Young, J. G. Verkade, *Polyhedron* **1995**, *14*, 393.
[21] Y. Saito, T. Yoshikawa, S. Bandow, M. Tomita, T. Hayashi, *Phys. Rev. B* **1993**, *48*, 1907.
[22] D. Briggs, M. P. Seah, *Practical Surface Analysis*, vol. 1. Wiley: Chichester, **1993**.
[23] C. Jones, E. Sammann, *Carbon* **1990**, *28*, 509.
[24] J. Meenan Brian, A. Hewitt Janet N. M. D. Brown, *Surf. Interface Anal.* **1992**, *18*, 187.
[25] C. D. Wagner, J. F. Moulder, L. E. Davis, W. M. Riggs, *Handbook of X-ray* Photoelectron Spectroscopy. Perkin Elmer, Physical Electronics.
[26] H. Ago, T. Kugler, F. Cacialli, W. R. Salaneck, M. S. P. Shaffer, A. H. Windle, R. H. Friend, *J. Phys. Chem. B* **1999**, *103*, 8116.
[27] C. Malitesta, G. Razzini, L Peraldo Bicelli, L. Sabbatini, *Int. J. Hydrogen Energy* **1987**, *12*, 219.
[28] Y. Baer, P. H. Citrin, G. K. Wertheim, *Phy. Rev. Lett.* **1976**, *37*, 49.
[29] R. Holm, *X-ray Photoelectron Spectroscopy*. Department of Applied Physics, Bayer AG, Leverkusen, pp. 37–72.
[30] P. W. Anderson, *Phys. Rev. Lett.* **1967**, *18*, 1049.
[31] G. D. Mahan, *Phys. Rev.* **1967**, *163*, 612.
[32] P. H. Citrin, G. K. Wertheim, Y. Baer, *Phys. Rev. B* **1977**, *16*, 4256.
[33] G. K. Wertheim, P. M. Th. M. Attekum, S. Basu, *Solid State Commun.* **1980**, *33*, 1127.
[34] S. Doniach, M. Sunjic, *J. Phys. C* **1970**, *3*, 285.
[35] P. H. Citrin, *Phys. Rev. B* **1973**, *8*, 5545.
[36] V. Weisskopf, E. Wigner, *Z. Phys.* **1930**, *63*, 54.
[37] A. Moisala, A. G. Nasibulin, E. I. Kauppinen, *J. Phys., Condens. Matter* **2003**, *15*, S3011.
[38] S. Maruyama, R. Kojima, Y. Miyauchi, S. Chiashi, M. Kohno, *Chem. Phys. Lett.* **2002**, *360*, 229.
[39] R. B. Maynard, Z. Wang, E. Sinn, R. N. Grimes, *Inorg. Chem.* **1983**, *22*, 873.
[40] K. Shimizu, H. Ishikawa, D. Takao, T. Yagi, K. Amaya, *Nature* **2002**, *419*, 597.
[41] V. V. Struzhkin, M. I. Eremets, W. Gan, H. K. Mao, R. J. Hemley, *Science* **2002**, *298*, 1213.
[42] A. Peigney, C. Laurent, E. Flahaut, R. R. Bacsa, A. Rousset, *Carbon* **2001**, *39*, 507.

